

Comparative study of adaptive variational quantum eigensolvers for multi-orbital impurity models

Anirban Mukherjee,¹ Noah F. Berthelsen,^{2,3,*} João C. Getelina,¹ Peter P. Orth,^{1,4,†} and Yong-Xin Yao^{1,4,‡}

¹*Ames Laboratory, U.S. Department of Energy, Ames, Iowa 50011, USA*

²*Ames Laboratory, Ames, Iowa 50011, USA*

³*Department of Electrical and Computer Engineering,
Iowa State University, Ames, Iowa 50011, USA*

⁴*Department of Physics and Astronomy, Iowa State University, Ames, Iowa 50011, USA*

We perform a systematic study of preparing ground states of correlated e_g and t_{2g} multi-orbital impurity models using variational quantum eigensolvers (VQEs). Both fixed and adaptive wavefunction ansätze are considered and the resulting gate depths and performance with and without quantum sampling noise are analyzed. We investigate the qubit adaptive derivative-assembled pseudo-trotter (ADAPT) VQE approach in the Hartree-Fock orbital basis, as well as the Hamiltonian variational ansatz (HVA) and an adaptive variant of it in the atomic orbital basis. An operator pool composed of pairwise commutators of the Hamiltonian terms is developed to allow a fair comparison between the adaptive and the fixed HVA ansatz. Using statevector simulations, we show that the most compact ansätze are obtained in the atomic orbital representation with symmetry-based Pauli tapering in parity encoding. We further perform adaptive VQE calculations including sampling noise, and demonstrate that high-fidelity state preparation can be achieved with the Hamiltonian commutator pool. By utilizing a doubly decomposed form of the impurity Hamiltonian and a noise resilient optimizer, we show that this approach requires only a modest number of about 2^{12} samples per energy evaluation. We discover a dichotomy of the operator pool complexity in the presence of quantum noise, where a small pool size reduces the adaptive overhead but a larger pool size accelerates the convergence to the ground state. Finally, we measure the ground state energy of the e_g model on IBM quantum hardware using the converged qubit-ADAPT ansatz, and obtain a relative error of 0.7% using error mitigation techniques including symmetry-filtering and zero-noise extrapolation.

I. INTRODUCTION

Eigenstate preparation for Hamiltonian systems is one promising application of noisy intermediate-scale quantum (NISQ) computers to achieve practical quantum advantage [1–7]. One of the representative hybrid quantum-classical algorithms to achieve this task is the variational quantum eigensolver (VQE). It attempts to find the ground state of a given Hamiltonian H within a variational manifold of states that are generated by parametrized quantum circuits $U(\boldsymbol{\theta})$ acting on a reference state $|\Psi_0\rangle$. The parameters $\boldsymbol{\theta}$ are obtained by classically minimizing the energy cost function $E(\boldsymbol{\theta}) = \langle\Psi_0|U^\dagger(\boldsymbol{\theta})HU(\boldsymbol{\theta})|\Psi_0\rangle$ that is measured on quantum hardware [2–4, 8]. The quality of a VQE calculation is tied to the ability of the variational ansatz to represent the ground state with high fidelity. In quantum computational chemistry, the unitary coupled cluster ansatz truncated at single and double excitations (UCCSD) has been extensively studied, owing to the success of the classical coupled cluster algorithm [9–11]. It was found that the application of UCCSD ansatz is limited by the rapid circuit growth with system size and the deteriorating accuracy in the presence of static electron correlations [8, 12, 13]. Therefore, alternative

variants have been developed, including hardware-efficient ansätze, that improve the scaling and expressibility of the wave function ansatz [3, 13–20].

Remarkably, it was found that compact and numerically exact variational ground state ansätze can be *adaptively* constructed for specific problems using approaches like the adaptive derivative-assembled pseudo-trotter (ADAPT) ansatz [13, 16]. The adaptive ansatz is typically obtained by successively appending parametrized unitaries to a variational circuit with generators chosen from a predefined operator pool. In practice, the ADAPT-VQE algorithm works well with an operator pool composed of fermionic excitation operators in the UCCSD ansatz. The extended qubit-ADAPT-VQE approach [16] utilizes an operator pool composed of Pauli strings in the qubit representation of fermionic excitation operators in the UCCSD ansatz, which is shown to be capable of generating more compact ansätze than the original ADAPT-VQE method at the price of introducing more variational parameters.

An alternative approach of constructing efficient wavefunction ansätze for problems in condensed matter physics is to exploit the sparsity of the Hamiltonian. Interacting electron systems are often simulated with reduced degrees of freedom, represented, for example, by a single-band Hubbard model. This simplified model features a sparse Hamiltonian including nearest-neighbor hopping and onsite Coulomb interactions only. Motivated by the simplicity of the Trotterized circuits for dynamics simulations due to Hamiltonian sparsity, the Hamiltonian variational ansatz (HVA) has been proposed by promoting

* Present address: Department of Computer Science, University of Maryland, College Park, MD, 20742, USA

† porth@iastate.edu

‡ ykent@iastate.edu

the time in Trotter circuits to independent variational parameters [21]. The HVA ansatz has attracted much attention and turns out to be very successful in reaching a compact state representation for sparse Hamiltonian system including local spin models [21–23]. Here, we propose to combine the flexibility of an adaptive approach with the efficiency of the HVA by designing a "Hamiltonian commutator" (HC) operator pool that contains pairwise commutators of operators that appear in the Hamiltonian.

To obtain a realistic description of materials, it is important to go beyond the single-band description of a simple Hubbard model [24]. A multi-orbital model including additional inter-orbital hoppings and Hund's couplings will necessarily make the Hamiltonian less sparse and consequently the HVA ansatz more complicated. On the other hand, quantum embedding methods are developed to reduce the material simulation complexity by mapping the infinite system to coupled subsystems, typically a noninteracting effective medium and some many-body interacting impurity models [24–31]. Therefore, the complexity is shifted from the solution of a full lattice system to that of multi-orbital impurity models, which can be more tractable with quantum computers [31].

In this paper, we compare the VQE circuit complexity for ground state preparation of multi-orbital many-body impurity models with a fixed HVA versus a qubit-ADAPT ansatz with different operator pools. An HC operator pool compatible with HVA is proposed to allow a fair comparison between qubit-ADAPT and fixed ansatz HVA calculations. For comparison, we also include results from UCCSD and qubit-ADAPT calculations with a simplified UCCSD pool. To connect with quantum embedding methods for realistic materials simulations, we use the Gutzwiller embedding approach [29, 32–37] to generate the impurity models that we employ for our benchmark [31, 38]. The quantum calculation we perform is general and could also be applied to other embedding methods. Numerical results from noiseless statevector simulator and quantum assembly language (QASM)-based simulator with quantum sampling noise are presented. Important techniques for efficient circuit simulations of qubit-ADAPT VQE are discussed. We also point out ways to simplify generators and reduce the operator pool size, and their impact on simulations. Finally, we investigate the impact of realistic noise by measuring the energy cost function of the e_g model composed of total 8 spin-orbitals on the IBM quantum processing unit (QPU) `ibmq_casablanca`.

The paper is organized as follows. Section II defines the quantum impurity models used for the comparative studies. The fixed ansätze, including UCCSD and HVA, and the associated operator pools for VQE and qubit-ADAPT calculations are explained in Sec. III. Section IV gives technical details on efficient circuit simulations, including low-rank tensor factorization and noise-resilient optimizer. The state vector and QASM simulation results are presented in Sec. V and VI. We discuss the effect of different

operator pools on qubit-ADAPT simulations in Sec. VII and benchmark realistic noise effects on QPU in Sec. VIII. The conclusion and outlook are given in Sec. IX.

II. QUANTUM EMBEDDING MODEL

Here we focus on a specific quantum embedding method: the well-established Gutzwiller variational embedding approach for correlated material simulations [29, 32–37], which is known to be equivalent to rotationally invariant slave-boson theory at the saddle point approximation [39, 40]. Recently, our group has developed a hybrid Gutzwiller quantum-classical embedding approach (GQCE) [31]. GQCE maps the ground state solution of a correlated electron lattice system to a coupled eigenvalue problem of a noninteracting quasiparticle Hamiltonian and one or multiple finite-size interacting embedding Hamiltonians [37]. Within GQCE one employs a quantum computer to find the ground state energy and single-particle density matrix of the interacting embedding Hamiltonian, for example, using VQE.

The embedding Hamiltonian describes an impurity model consisting of a physical many-body N_S -orbital subsystem ($\hat{\mathcal{H}}_S$) coupled with a N_B -orbital quadratic bath ($\hat{\mathcal{H}}_B$):

$$\hat{\mathcal{H}} = \hat{\mathcal{H}}_S + \hat{\mathcal{H}}_B + \hat{\mathcal{H}}_{SB}, \quad (1)$$

with

$$\begin{aligned} \hat{\mathcal{H}}_S = & \sum_{\alpha\beta} \sum_{\sigma} \epsilon_{\alpha\beta} \hat{c}_{\alpha\sigma}^{\dagger} \hat{c}_{\beta\sigma} \\ & + \frac{1}{2} \sum_{\alpha\beta\gamma\delta} \sum_{\sigma\sigma'} V_{\alpha\beta\gamma\delta} \hat{c}_{\alpha\sigma}^{\dagger} \hat{c}_{\gamma\sigma'}^{\dagger} \hat{c}_{\delta\sigma'} \hat{c}_{\beta\sigma}, \end{aligned} \quad (2)$$

$$\hat{\mathcal{H}}_B = - \sum_{ab} \sum_{\sigma} \lambda_{ab} \hat{f}_{a\sigma}^{\dagger} \hat{f}_{b\sigma}, \quad (3)$$

$$\hat{\mathcal{H}}_{SB} = \sum_{a\alpha} \sum_{\sigma} \left(\mathcal{D}_{a\alpha} \hat{c}_{a\sigma}^{\dagger} \hat{f}_{a\sigma} + h.c. \right). \quad (4)$$

Here $\alpha, \beta, \gamma, \delta$ are composite indices for sites and spatial orbitals in the physical subsystem. Likewise, the bath sites and orbitals are labelled by a, b , and σ is the spin index. The fermionic ladder operators \hat{c} and \hat{f} are used to distinguish the physical and bath orbital sites. The one-body component and two-body Coulomb interaction in the physical subsystem are specified by matrix ϵ and tensor V . The quadratic bath and its coupling to the subsystem are defined by matrix λ and \mathcal{D} , respectively. Compared with typical quantum chemistry calculations, the embedding Hamiltonian is much sparser since the two-body interaction only exists between electrons in the physical subsystem. For clarification, we name the above defined embedding Hamiltonian system as (N_S, N_B) impurity model, where (N_S, N_B) are the number of spatial orbitals in the system and bath models. Within GQCE, the ground state solution of the embedding Hamiltonian

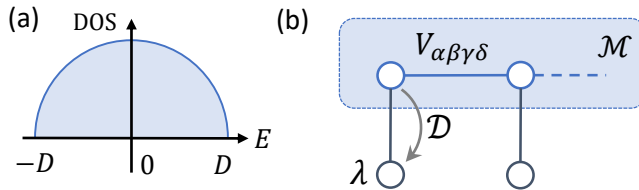


FIG. 1. **Model setup.** (a) The noninteracting density of states (DOS) of the degenerate multi-band Hubbard-Hund lattice model on the Bethe lattice has semicircular shape. (b) $(\mathcal{M}, \mathcal{M})$ site impurity model with \mathcal{M} -fold degenerate correlated orbitals coupled with \mathcal{M} bath orbitals. The interactions among the physical orbitals are specified by the Coulomb matrix V . Due to symmetry, each physical orbital (positioned at zero energy level) is coupled with a single bath orbital at energy level λ with a coupling parameter \mathcal{D} .

at half electron filling is needed, which is achieved by a chemical potential absorbed in the one-body Hamiltonian coefficient matrices ϵ and λ in Eq. (1).

In the numerical simulations presented here, we choose a Gutzwiller embedding Hamiltonian for the degenerate \mathcal{M} -band Hubbard model. The noninteracting density of states of the lattice model adopts a semi-circular form $\rho(\omega) = \frac{2\mathcal{M}}{\pi D} \sqrt{1 - (\omega/D)^2}$ as shown in Fig. 1(a), which corresponds to the Bethe lattice in infinite dimensions. We set the half band width $D = 1$ as the energy unit. In physical systems D is of the order of a few eV. The Coulomb matrix V takes the Kanamori form specified by Hubbard U and Hund's J parameters: $V_{\alpha\alpha\alpha\alpha} = U$, $V_{\alpha\alpha\beta\beta} = U - 2J$, and $V_{\alpha\beta\alpha\beta} = V_{\alpha\beta\beta\alpha} = J$ for $\alpha \neq \beta$. Here we have assumed spin and orbital rotational invariance (within the e_g or t_{2g} manifold) for simplicity and to limit the interaction parameter space. The embedding Hamiltonian, as illustrated in Fig. 1(b), is represented with $2\mathcal{M}$ spatial orbitals: \mathcal{M} degenerate physical orbital plus \mathcal{M} degenerate bath orbitals. The symmetry of the model reduces matrices ϵ , λ and \mathcal{D} to single parameters proportional to identity. In the following, we set the electron filling for the lattice model to $\mathcal{M} + 1$, which is one unit larger than half-filling, and fix the ratio of the Hund's to Hubbard interaction to $J/U = 0.3$. These parameters can describe the physics of correlation-induced bad metallic states in multi-band correlated materials such as chalcogenides FeSe and FeTe[41]. In calculations below, we consider $\mathcal{M} = 2$ and $\mathcal{M} = 3$, which correspond to e_g and t_{2g} orbitals in cubic crystal symmetry, respectively. The associated $(N_S, N_B) = (2, 2)$ and $(3, 3)$ impurity models have in total 8 and 12 spin-orbitals. In quantum simulations reported below, parity encoding which exploits the symmetry in total number of electrons and spin z-component is adopted to transform the fermionic Hamiltonian to qubit representation.

III. METHODS: VARIATIONAL QUANTUM EIGENSOLVERS

GQCE leverages quantum computing technologies to solve for the ground state of the embedding Hamiltonian, specifically the energy and one-particle density matrix. Note that the ground state is always prepared at half-filling for the embedding system, which is determined by the Gutzwiller embedding algorithm and is independent of the actual electron filling of the physical lattice model [29, 37]. For this purpose, we benchmark multiple versions of VQE with fixed or adaptively generated ansatz to prepare the ground state of the above embedding Hamiltonian. We consider VQE calculations with fixed UCCSD ansatz and the associated qubit-ADAPT VQE using a simplified UCCSD operator pool. The calculations are naturally performed in the molecular orbital (MO) basis representation, where the reference Hartree-Fock (HF) state becomes a simple tensor product state and fermionic excitation operators can be naturally defined. However, using a MO representation comes at the cost of reducing the sparsity of the embedding Hamiltonian compared to the atomic orbital (AO) basis representation. To take advantage of the Hamiltonian sparsity in AO representation, we consider a generalized form of the HVA, and the associated qubit-ADAPT VQE with a modified HC operator pool.

A. VQE-UCCSD method

For an N_q -qubit system with Hamiltonian $\hat{\mathcal{H}}$, VQE amounts to minimizing the cost function $E(\boldsymbol{\theta}) = \langle \Psi[\boldsymbol{\theta}] | \hat{\mathcal{H}} | \Psi[\boldsymbol{\theta}] \rangle$ with respect to the variational parameters $\boldsymbol{\theta}$. Here, $|\Psi[\boldsymbol{\theta}]\rangle = U(\boldsymbol{\theta})|\Psi_0\rangle$ is obtained by application of a parametrized quantum circuit $U(\boldsymbol{\theta})$ onto a reference state $|\Psi_0\rangle$. The cost function is evaluated on a quantum computer and the optimization is performed classically using $E(\boldsymbol{\theta})$ as input. The accuracy of VQE is therefore tied to the variational ansatz $|\Psi[\boldsymbol{\theta}]\rangle$ and to the performance of the classical optimization, e.g., how often the cost function is called during the optimization and how well the approach converges to the global (as opposed to a local) minimum of $E(\boldsymbol{\theta})$. The UCCSD ansatz takes the following form:

$$|\Psi[\boldsymbol{\theta}]\rangle = e^{\hat{T}[\boldsymbol{\theta}] - \hat{T}^\dagger[\boldsymbol{\theta}]} |\Psi_0\rangle = e^{-i \sum_j \theta_j f_j(\{\hat{\sigma}\})} |\Psi_0\rangle. \quad (5)$$

The operator $\hat{T}[\boldsymbol{\theta}]$ consists of single and double excitation operators with respect to the HF reference state $|\Psi_0\rangle$:

$$\hat{T}[\boldsymbol{\theta}] = \sum_{p\bar{p}} \theta_p^{\bar{p}} \hat{c}_p^\dagger \hat{c}_p + \sum_{p < q, \bar{p} < \bar{q}} \theta_{pq}^{\bar{p}\bar{q}} \hat{c}_p^\dagger \hat{c}_{\bar{q}}^\dagger \hat{c}_{\bar{q}} \hat{c}_p. \quad (6)$$

Here p, q and \bar{p}, \bar{q} refer to the occupied and unoccupied MOs, respectively, with spin included implicitly. $f_j(\{\hat{\sigma}\}) = \sum_k w_{jk} \hat{P}_k$ is a weighted sum of Pauli strings

$(\hat{P}_k \in \{I, X, Y, Z\}^{\otimes N_q})$ for the qubit representation of the fermionic excitation operator associated with parameter θ_j . Here θ_j run over the set of parameters $\theta_p^{\bar{p}}$ and $\theta_{pq}^{\bar{p}\bar{q}}$. For the impurity model without spin-orbit interaction, only excitation operators which conserve respective number of electrons in the spin-up and spin-down sectors need to be considered. In practical implementation, a single step Trotter approximation is often adopted to construct the UCCSD circuit:

$$|\Psi[\theta]\rangle \approx \prod_{jk} e^{-i\theta_j w_{jk} \hat{P}_k} |\Psi_0\rangle. \quad (7)$$

Furthermore, the final circuit state generally depends on the order of the unitary gates. In calculations reported here, we apply gates with single-excitation operators first following the implementation in Qiskit [42].

B. Qubit-ADAPT VQE with simplified UCCSD pool

VQE-UCCSD is a useful reference point for quantum chemistry calculations. However, the fixed UCCSD ansatz has limited accuracy and often involves deep quantum circuits for implementations. Various approaches have been proposed to construct more compact variational ansatz with systematically improvable accuracy. In this work, we will focus on the qubit-ADAPT VQE method [16], where the ansatz takes a similar pseudo-Trotter form:

$$|\Psi[\theta]\rangle = \prod_{j=1}^{N_\theta} e^{-i\theta_j \hat{P}_j} |\Psi_0\rangle. \quad (8)$$

With qubit-ADAPT, the ansatz is recursively expanded by adding one unitary at a time, followed by reoptimization of parameters. The additional unitary is constructed with a generator selected from a predefined Pauli string pool which gives maximal energy gradient amplitude $|g|_{\max}$ at the preceding ansatz state. The ansatz expansion process iterates until convergence, which is set by $|g|_{\max} < 10^{-4}$ here. Note that we have set the half bandwidth of the original noninteracting lattice model to $D = 1$, such that $|g|_{\max} \sim 0.1$ meV in physical systems with $D \sim 1$ eV.

The computational complexity of qubit-ADAPT VQE calculations is tied to the size of the operator pool, which consists of a set of Pauli strings. Naturally, one can construct an operator pool using all the Pauli strings in the qubit representation of fermionic single and double excitation operators. However, the dimension of this UCCSD-compatible pool is usually quite big and scales as $\mathcal{O}(N_q^4)$. Here we propose a much simplified operator pool, which consists of Pauli strings from single excitation and paired double excitation operators only. The pair excitation involves a pair of electrons with opposite spins, which are initially occupying the same spatial MO, hopping together to another initially unoccupied spatial MO. To further reduce the circuit depth, only one

Pauli string is chosen from each qubit representation of the fermionic excitation operator. The qubit representation is a weighted sum of equal-length Pauli strings, and a specific choice of which one of them does not seem to be important in practical calculations reported here. This simplified pool containing operators arising from the UCC ansatz restricted to single and paired double excitation operators (sUCCSpD)[43, 44] greatly reduces the number of Pauli strings compared to the UCCSD pool. The dimension of this sUCCSpD pool scales as $\mathcal{O}(N_q^2)$. For the (2, 2) e_g impurity model, the pool size reduces from 152 for UCCSD to 56 for sUCCSpD, and for the (3, 3) t_{2g} impurity model it reduces from 828 to 192. The code to perform the above qubit-ADAPT VQE calculations at statevector level with examples are available at figshare [45].

C. Hamiltonian Variational Ansatz

The Hamiltonian sparsity in the AO basis naturally motivates the application of the Hamiltonian variational ansatz (HVA)[21], which generally takes a form of multi-layer Trotterized annealing-like circuits. While different ways of designing specific HVA forms have been developed, we propose the following ansatz with L layers for the impurity model:

$$|\Psi[\theta]\rangle = \prod_{l=1}^L \prod_j e^{-i\theta_{lj} \hat{h}_j} |\Psi_0\rangle. \quad (9)$$

Here $\hat{\mathcal{H}} = \sum_j \hat{h}_j$, with \hat{h}_j being a subgroup of Hamiltonian terms which share the same coefficient and mutually commute. Such ansatz construction aims to differentiate the physical and bath orbitals, while retaining the degeneracy information among the orbitals in a systematic way. For each layer of unitaries, we first apply the multi-qubit rotations that are generated by the interacting part of the Hamiltonian, since these act as entangling gates. For the $(\mathcal{M}, \mathcal{M})$ impurity model, two reference states have been tried: $|\Psi_0^{(I)}\rangle$ is a simple tensor product state with \mathcal{M} physical orbitals fully occupied and the bath orbitals empty; $|\Psi_0^{(II)}\rangle$ is the ground state of the noninteracting part of $\hat{\mathcal{H}}$, which is equivalent to the one-electron core Hamiltonian in quantum chemistry. We did not find any significant difference between the two choices of reference state in practical simulations of the impurity models. Therefore, only HVA calculations with the reference state $|\Psi_0^{(I)}\rangle$ are reported here. We adopt the gradient-based Broyden–Fletcher–Goldfarb–Shanno (BFGS) algorithm as the classical optimizer. Proper parameter initialization for HVA optimization is crucial, as barren plateaus and local energy minima are generally present in the variational energy landscape. In practice, we find that a uniform initialization of the parameters, such as setting all to $\pi/7$, overall works well for simulations reported here.

Inspired by the idea of adaptive ansatz generation [13], we also tried constructing and optimizing an L -layer HVA ansatz by adaptively adding layers from 1 to L . Specifically, the calculation starts with optimizing a single-layer ansatz, followed by appending another layer to the ansatz while keeping the first layer at previously obtained optimal angles. The two-layer ansatz is then optimized with the parameters for the new layer initialized randomly or uniformly. The procedure continues with the optimization of l -layer ansatz leveraging the $(l-1)$ -layer solution until the ansatz reaches L layers. Let the number of cost function evaluations for optimizing an l -layer ansatz be $N_l^{(2)}$. The total number of function evaluations amounts to $N^{(2)} = \sum_{l=1}^L N_l^{(2)}$. In practice, we find that the direct optimization of the L -layer ansatz using a uniform initialization takes $N^{(1)}$ function evaluations with $N^{(1)} \sim N_L < N^{(2)}$, where N_L is the number of variational parameters per layer, and reaches the same accuracy. Starting with L layers is therefore more efficient than growing the ansatz layer by layer. The code to perform the above HVA calculations at statevector level with examples are available at figshare [46].

D. Hamiltonian Commutator Pool

It has been demonstrated that the qubit-ADAPT VQE in the MO basis outperforms VQE-UCCSD calculations regarding circuit complexity and numerical accuracy [13, 16]. Therefore, it is interesting to compare the corresponding qubit-ADAPT VQE with Hamiltonian-compatible pool in AO basis and HVA calculations. Following HVA, we choose the simple tensor product state $|\Psi_0^{(1)}\rangle$ as the reference state. In qubit-ADAPT step, the energy gradient criterion $g_\theta = 2 \operatorname{Im}[\langle \Psi[\theta] | \hat{P} \hat{\mathcal{H}} | \Psi[\theta] \rangle]$ to append a new unitary generated by \hat{P} vanishes due to symmetry with $\Psi[\theta]$, if the number of Pauli- Y operators in the Pauli string \hat{P} is even [13, 47]. This can be simply shown from the following argument. Because the impurity model in this study respects time reversal symmetry and spin-flip (Z_2) symmetry, both Hamiltonian $\hat{\mathcal{H}}$ and wavefunction are real ($\hat{\mathcal{H}} = \hat{\mathcal{H}}^*$, $\Psi[\theta] = \Psi[\theta]^*$). The Pauli string \hat{P} is also real ($\hat{P} = \hat{P}^*$) if it has an even number of Pauli- Y operators. Consequently, the expectation value of $\langle \Psi[\theta] | \hat{P} \hat{\mathcal{H}} | \Psi[\theta] \rangle$ is real and g_θ vanishes if the associated generator \hat{P} has an even number of Pauli- Y operators.

By construction, the sUCCSpD pool consists of Pauli strings of odd number of Y 's. However, the Hamiltonian of the impurity models studied here are all real. Consequently, all the Pauli strings in the qubit representation of the Hamiltonian contain an even number of Y 's, which excludes the option of directly constructing the operator pool from the Hamiltonian operators. Nevertheless, the practical usefulness of HVA implies that the Hamiltonian-like pool can be constructed by commuting the Hamiltonian terms, which we call Hamiltonian commutator (HC) pool \mathcal{P}_{HC} . Mathematically \mathcal{P}_{HC} is

constructed in the following manner,

$$\mathcal{P}_{\text{HC}} = \left\{ \frac{1}{2i} [\hat{P}, \hat{P}'] \mid \hat{P}, \hat{P}' \in \mathcal{P}_{\text{H}}, \text{ and } N_Y([\hat{P}, \hat{P}']) \pmod{2} = 1 \right\}, \quad (10)$$

Here \mathcal{P}_{H} is the set of Pauli strings $\{\hat{P}_h\}$ present in the qubit representation of Hamiltonian $\hat{\mathcal{H}} = \sum_h w_h \hat{P}_h$. $N_Y(\hat{P})$ counts the number of Y operators in the Pauli string \hat{P} . Therefore, the size of \mathcal{P}_{HC} can scale as N_{H}^2 , where N_{H} is the total number of Hamiltonian terms. Clearly, the pool \mathcal{P}_{HC} should only be applied to sparse Hamiltonian systems. The dimension of the HC pool is 56 for the e_g impurity model, and 192 for the t_{2g} model.

IV. QUANTUM CIRCUIT IMPLEMENTATION TECHNIQUES

Performing a calculation on a quantum computer always needs to deal with the presence of noise. Even for ideal fault-tolerant quantum computers, quantum sampling (or shot) noise is present due to finite number of measurements that is used to estimate expectation values. The current noisy quantum devices exhibit additional noise originating from qubit relaxation and dephasing as well as hardware imperfections when implementing unitary gate operations. In this section, we describe several techniques adopted in our simulations to most efficiently use the available quantum resources and stabilize the calculations against noise. In this section, we focus on the impact of sampling noise. In Sec. VIII we discuss how to mitigate gate noise.

A. Measurement circuit reduction

The quantum circuit implementation for VQE and its adaptive version amounts to the direct measurement of the Hamiltonian as a weighted sum of Pauli string expectation values, $\langle \hat{\mathcal{H}} \rangle = \sum_h w_h \langle \hat{P}_h \rangle$, with respect to parametrized circuits $U[\theta]$. Here, $\hat{\mathcal{H}} = \sum_h w_h \hat{P}_h$ is the Hamiltonian in qubit representation. Because the number of shots (or repeated measurements) scales with the desired precision ϵ as $N_{\text{sh}} \propto \frac{1}{\epsilon^2}$ due to central limit theorem, N_{sh} is often huge in practical calculations. Therefore, it is desirable to group the Pauli strings into mutually commuting sets such that the number of distinct measurement circuits is reduced to minimum. Indeed, many techniques to achieve such measurement reduction have been developed [48–53]. In this work, we adopt the measurement reduction strategy based on the Hamiltonian integral factorization [53], which shows a favorable linear system-size scaling of the number of distinct measurement circuits and embraces a diagonal representation for the operators to be measured.

Specifically, we transform the physical subsystem Hamil-

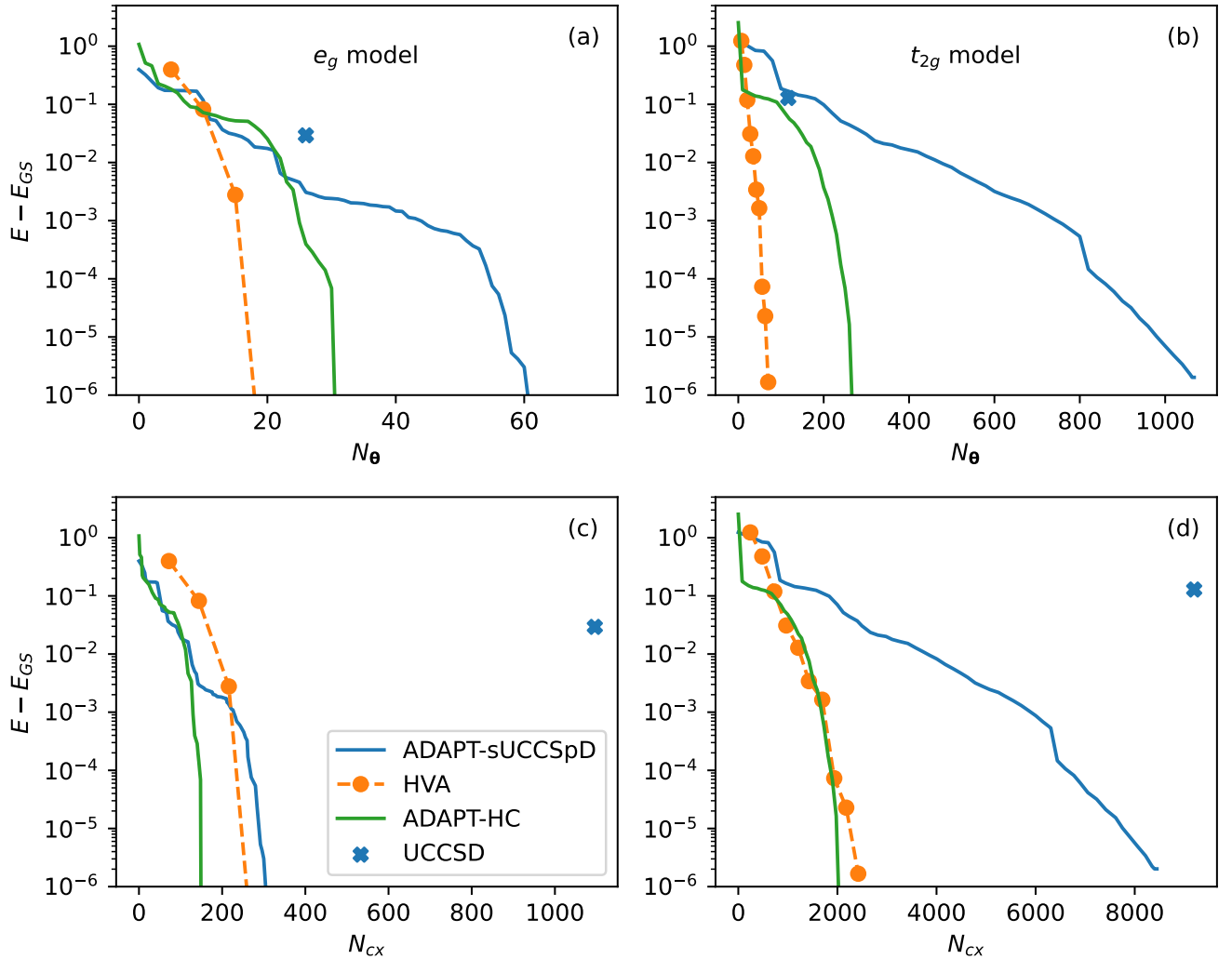


FIG. 2. **Energy convergence of VQE calculations with four types of ansätze.** Panels (a,b) show the energy difference between the variational and the exact ground state energy E_{GS} as a function of number of variational parameters N_θ . The lower panels (c, d) show the energy difference versus the number of CNOT gates N_{cx} . Panels (a,c) are for the degenerate ($N_S = 2, N_B = 2$) e_g impurity model and panels (b,d) correspond to the (3, 3) t_{2g} impurity model. VQE calculations are reported with fixed HVA and UCCSD ansatz as well as with adaptive ansatzes constructed from a sUCCSpD pool and a Hamiltonian commutator pool. Here N_{cx} is estimated according to each multi-qubit rotation gate with a Pauli string generator P of length l contributing $2(l - 1)$ CNOT gates, which assumes full qubit connection. The Hamiltonian parameters are $\epsilon = -9.8(-12.7)$, $\lambda = 0.3(0.1)$, $\mathcal{D} = -0.3(-0.3)$ with the same Hubbard $U = 7$ for the e_g (t_{2g}) model, corresponding to the correlated bad metallic regime.

tonian as follows:

$$\hat{\mathcal{H}}_S = \sum_{\alpha\beta\sigma} \tilde{\epsilon}_{\alpha\beta} \hat{c}_{\alpha\sigma}^\dagger \hat{c}_{\beta\sigma} + \frac{1}{2} \sum_{\alpha\beta\gamma\delta} \sum_{\sigma\sigma'} V_{\alpha\beta\gamma\delta} \hat{c}_{\alpha\sigma}^\dagger \hat{c}_{\beta\sigma} \hat{c}_{\gamma\sigma'}^\dagger \hat{c}_{\delta\sigma'}, \quad (11)$$

with $\tilde{\epsilon}_{\alpha\beta} = \epsilon_{\alpha\beta} - \frac{1}{2} \sum_\gamma V_{\alpha\gamma\gamma\beta}$. A typical way to simplify the measurement of the two-body terms $\hat{\mathcal{H}}_S^{(2)}$ in Eq. (11) is to perform nested matrix factorization for the Coulomb V tensor. Namely, we first rewrite $\hat{\mathcal{H}}_S^{(2)}$ in the following factorized form by diagonalizing the real symmetric

positive semidefinite supermatrix $V_{(\alpha\beta),(\gamma\delta)}$:

$$\hat{\mathcal{H}}_S^{(2)} = \frac{1}{2} \sum_{l=1}^L \sum_{\alpha\beta} \sum_{\sigma} \left(\mathcal{L}_{\alpha\beta}^{(l)} \hat{c}_{\alpha\sigma}^\dagger \hat{c}_{\beta\sigma} \right)^2. \quad (12)$$

Here l runs through the L positive eigenvalues of the supermatrix V , and the l th component of the auxiliary tensor \mathcal{L} is obtained by multiplying the l th eigenvector with the square root of l th positive eigenvalue. Each tensor component, $\mathcal{L}^{(l)}$, which is a real symmetric matrix, is subsequently diagonalized to reach the following

decomposition:

$$\begin{aligned} \sum_{\alpha\beta\sigma} \mathcal{L}_{\alpha\beta}^{(l)} \hat{c}_{\alpha\sigma}^\dagger \hat{c}_{\beta\sigma} &= \sum_{m=1}^{M_l} \lambda_m^{(l)} \sum_{\alpha\beta\sigma} U_{\alpha m}^{(l)} U_{\beta m}^{(l)} \hat{c}_{\alpha\sigma}^\dagger \hat{c}_{\beta\sigma} \\ &= \sum_{m=1}^{M_l} \sum_{\sigma} \lambda_m^{(l)} \hat{n}_{m\sigma}^{(l)} \end{aligned} \quad (13)$$

Here, we have defined $\hat{n}_{m\sigma}^{(l)} \equiv \sum_{\alpha\beta} U_{\alpha m}^{(l)} U_{\beta m}^{(l)} \hat{c}_{\alpha\sigma}^\dagger \hat{c}_{\beta\sigma}$. The index m goes through the M_l nonzero eigenvalues $\lambda_m^{(l)}$ and associated eigenvectors $U_m^{(l)}$, which determines the single-particle basis transformation for the l th component. The whole embedding Hamiltonian of Eq. (1) can then be cast into the following doubly-factorized form with a unitary transformation similar to Eq. (13) for the one-body part:

$$\hat{\mathcal{H}} = \sum_{m=1}^{M_0} \sum_{\sigma} \epsilon_m^{(0)} \hat{n}_{m\sigma}^{(0)} + \frac{1}{2} \sum_{l=1}^L \sum_{m=1}^{M_l} \sum_{\sigma} \left(\lambda_m^{(l)} \hat{n}_{m\sigma}^{(l)} \right)^2, \quad (14)$$

which is composed of $L+1$ groups characterized by unique single-particle basis transformations $\{U^{(l)}\}$, including one from the single-electron component. This form allows efficient measurement of the Hamiltonian expectation value using $L+1 \propto \mathcal{O}(N)$ distinct circuits for a generic quantum chemistry problem with single-particle basis dimension given by N .

The expectation value of $\hat{\mathcal{H}}$ is obtained by measuring each group l independently in the variational state $|\Psi[\theta]\rangle$. The variational state is transformed to the same representation used in the l th group by applying a series of Givens rotations, $\{e^{\theta_{\mu\nu}(\hat{c}_{\mu\sigma}^\dagger \hat{c}_{\nu\sigma} - h.c.)}\}$, with the set of $\{\theta_{\mu\nu}\}$ determined by the single-particle transformation matrix $U^{(l)}$. Here μ and ν are generic indices for physical and bath orbital sites. Therefore, the number of distinct measurement circuits is $N_c = L+1$. As an example, we have $N_c = 4$ for e_g model. We refer to Appendix A for further details.

In practice, it is advantageous to isolate the one-body and two-body terms that contain only density operators before the double factorization procedure, because they are already in a diagonal representation. For the e_g model we have carried out the double-factorization with explicit calculations in Appendix A and we ultimately find $N_c = 3$ for the e_g model. This can be compared with the Hamiltonian measurement procedure using the mutual qubit-wise commuting groups: operators that commute with respect to every qubit site are placed in the same group. This commuting Pauli approach generally needs $N_c \propto \mathcal{O}(N^4)$ distinct circuits for Hamiltonian measurement. And for the e_g model, it requires $N_c = 5$.

B. Noise-resilient optimization

Although classical optimization approaches such as BFGS, which rely on a computation of the energy gradient, are effective, they rely on very accurate cost function

evaluations. Because of the inherent noise in quantum computing, optimization algorithms that are robust to cost function noise are highly desirable. In the noisy quantum simulations reported here, we adopt two optimization techniques which are more tolerant to noise than BFGS: the sequential minimal optimization (SMO)[54] and *Adadelta*. Because of their similar performance in the noisy simulations, we only discuss SMO in the main text, and leave the discussions of *Adadelta* in Appendix B.

SMO is the first technique we use for our noisy quantum simulations. Tailored to the qubit-ADAPT ansatz of Eq. (8) where each variational parameter is associated with a single Pauli string generator, the optimization consists of N_{sw} sweeps of sequential single parameter minimization of the cost function. At a specific optimization step with varying parameter θ_j while keeping others fixed, the cost function has a simple form of $a \cos(2\theta_j - b) + c$, with the optimal $\theta_j^* = b/2$ if $a < 0$ and $(b+\pi)/2$ otherwise. To determine the parameters a, b, c , one requires knowledge of function values for at least three mesh points in the range of $[-\pi/2, \pi/2]$. In practice, we use eight uniformly spaced mesh points to better mitigate the effect of noise in the cost function. Consequently, least square fitting is used to determine the values of a, b and c . In SMO calculations, we use the number of sweeps as the parameter to control the convergence, which we set to $N_{\text{sw}} = 40$. Alternative control parameters, such as energy and gradient, usually are required to be evaluated at higher precision, which can be challenging and introduce additional quantum computation overhead.

In this work, the noisy simulations with classical optimizations only include quantum noise due to finite number of measurements or shots (N_{sh}). The purpose is to investigate the performance of the qubit-ADAPT algorithm in the presence of this shot noise, which is controlled by a single parameter N_{sh} . The code with the circuit implementation of qubit-ADAPT VQE with examples on QASM simulator and quantum hardware are available at figshare [55].

V. STATE VECTOR SIMULATIONS

In this section we present numerical simulation results using a state vector simulator, which is equivalent to a fault-tolerant quantum computer with an infinite number of measurements ($N_{\text{sh}} = \infty$). Figure 2 shows the ground state energy calculations of the $(2, 2)$ e_g and $(3, 3)$ t_{2g} impurity models using VQE-HVA as well as qubit-ADAPT VQE with sUCCSpD and HC pools. The reference UCCSD energy is 0.029 higher than the exact ground state energy E_{GS} for the e_g model and 0.128 higher for the t_{2g} model. This implies that both models are in the strong electron correlation region. For calculations of the e_g model, the energy converges below 10^{-5} with $N_{\theta} = 20$ variational parameters for VQE-HVA, $N_{\theta} = 59$ for ADAPT-sUCCSpD, and $N_{\theta} = 31$ for ADAPT-HC. Although the qubit-ADAPT VQE calculation on a statevec-

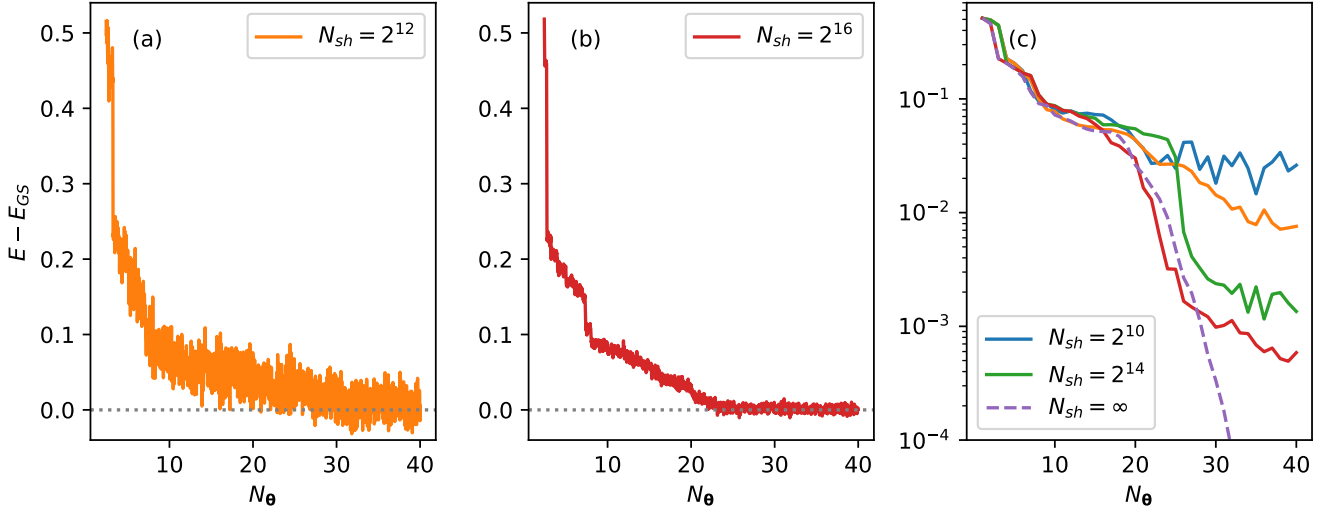


FIG. 3. **Energy convergence of qubit-ADAPT VQE noisy simulations of $(2,2)$ e_g model with SMO optimizer.** The difference between the exact ground state energy E_{GS} and qubit-ADAPT VQE noisy simulation results, obtained with number of shots $N_{sh} = 2^{12}$ in panel (a) and $N_{sh} = 2^{16}$ in panel (b). Panel (c) shows the energy differences evaluated using state vector for the adaptive ansätze obtained in the noisy simulations, with $N_{sh} = 2^{10}, 2^{12}, 2^{14}$ and 2^{16} . The state vector simulation results ($N_{sh} = \infty$) of the qubit-ADAPT VQE are also shown in dashed line for reference. Hamiltonian parameters are identical to those used in Fig. 2.

tor simulator is in principle deterministic, the operator selection from a predefined operator pool can introduce some randomness due to the numerical accuracy and near degeneracy of scores (i.e., the associated gradient components) for some operators. As a result, the converged N_θ can slightly change by about one between runs.

As a simple estimation of the circuit complexity for NISQ devices, we provide the number of CNOT gates N_{cx} assuming full qubit connectivity, which can be realized in trapped ion systems. The converged circuit has $N_{cx} = 288$ for VQE-HVA, $N_{cx} = 292$ for ADAPT-sUCCSpD, and $N_{cx} = 150$ for ADAPT-HC. As a reference, the UCCSD ansatz has $N_\theta = 26$ and $N_{cx} = 1096$. The HVA calculation converges with the smallest number of variational parameters, but the number of CNOT gates (N_{cx}) is in between that of ADAPT-HC and ADAPT-sUCCSpD, because each variational parameter in HVA is associated with a generator composed of a weighted sum of Pauli strings. The ADAPT-HC calculation starts from a reference state $|\Psi_0^{(I)}\rangle$, a simple tensor product state in AO basis, with energy higher than the HF reference state used by ADAPT-sUCCSpD, yet ADAPT-HC converges faster to the ground state. In fact, the initial state fidelity, defined as $f \equiv |\langle \Psi_0 | \Psi_{GS} \rangle|^2$, is 0.19 for ADAPT-HC, compared with 0.76 for ADAPT-sUCCSpD. Therefore, the final ansatz complexity does not show a simple positive correlation with the initial state fidelity, which implies that both the Hamiltonian structure and operator pool are determining factors.

Compared with ADAPT-sUCCSpD, the advantage of ADAPT-HC becomes more prominent when applied to

the t_{2g} model. To reach energy convergence below 10^{-5} , ADAPT-HC needs $N_\theta = 270$ parameters and $N_{cx} = 2052$ CNOTs, while ADAPT-sUCCSpD requires as many as $N_\theta = 1020$ parameters and $N_{cx} = 8066$ CNOTs. For reference, the UCCSD ansatz has $N_\theta = 117$ parameters and $N_{cx} = 9200$ CNOTs. The HVA calculation is carried out with up to $L = 10$ layers, which amounts to $N_\theta = 70$ and $N_{cx} = 2420$, and the energy converges close to 10^{-6} .

VI. QUANTUM SIMULATIONS WITH SHOT NOISE

The ADAPT VQE calculations are often reported at the state vector level, and a systematic study including the effect of noise is not yet available [13, 16, 56–58]. Here we present qubit-ADAPT VQE calculations of the $(2,2)$ e_g model including shot noise.

Figure 3 shows the representative convergence behavior of the qubit-ADAPT energy with an increasing number of variational parameters N_θ calculated using different number of shots per observable measurement: panel (a) is for $N_{sh} = 2^{12}$, and panel (b) is for $N_{sh} = 2^{16}$. We use SMO for the classical optimization. The adaptive ansatz energy E overall decreases as the circuit grows and more variational parameters are used. The energy uncertainty is tied to the number of shots N_{sh} . The energy spread roughly reduces by a factor of 4 when N_{sh} increases from 2^{12} (a) to 2^{16} (b), consistent with the 16-fold increase in N_{sh} due to central limit theorem. The energy points shown include not only the final SMO optimized energies

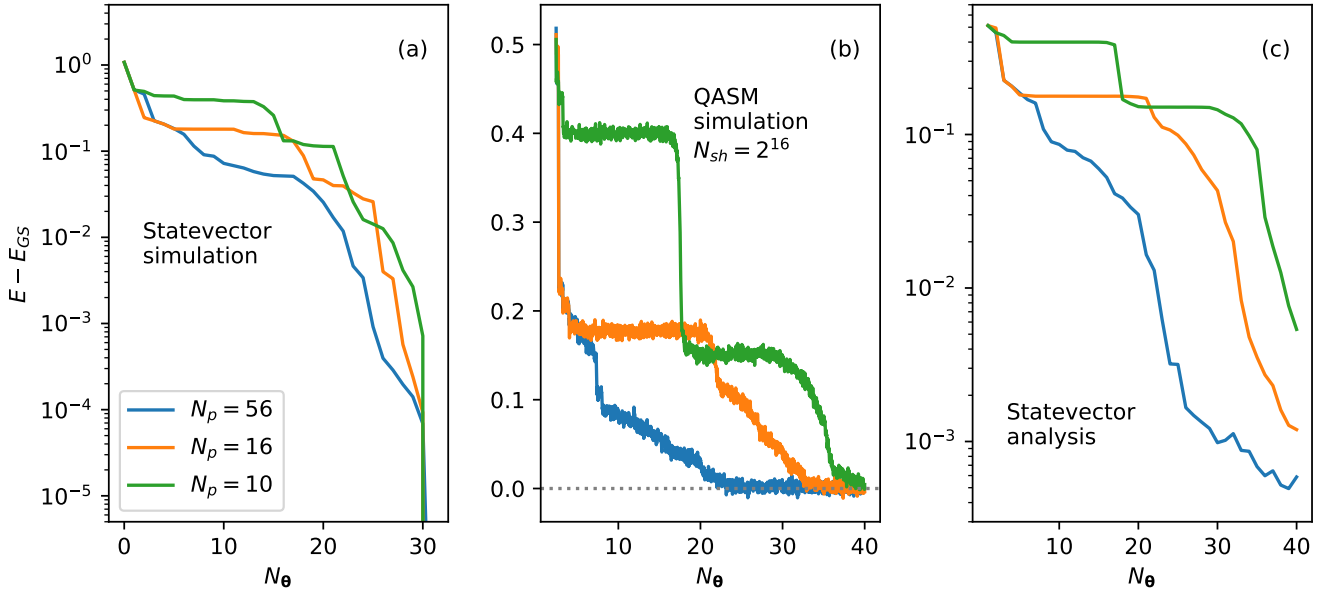


FIG. 4. **Pool size dependence of the energy convergence behavior for qubit-ADAPT VQE calculations of the e_g model.** The difference between the exact ground state energy E_{GS} and qubit-ADAPT results as a function of N_θ from (a) state vector simulations and (b) QASM simulations with $N_{sh} = 2^{16}$ shots using three different operator pools of size 56, 16 and 10, derived from the Hamiltonian commutator pool. The respective energy differences evaluated using state vector for the adaptive ansaetze obtained in the noisy simulations of panel (b) are shown in panel (c).

of the qubit-ADAPT ansatz with N_θ parameters, but also the intermediate energies after each of the $N_{sw} = 40$ sweeps during SMO optimizations to provide more detailed convergence information. The above reported N_{sh} is referred to measurements for SMO optimizations. At the operator screening step of the qubit-ADAPT calculation to expand the ansatz by appending an additional optimal unitary, we fix $N_{sh} = 2^{16}$ shots for energy evaluations in all cases, and determine the energy gradient by the parameter-shift rule [59].

To further assess the quality of the qubit-ADAPT ansatz obtained in noisy simulations, in Fig. 3(c) we plot the ansatz energies evaluated using state vector at the end of each noisy SMO optimization. The four solid curves are calculated using the variational parameters that are obtained by noisy optimizations with different numbers of shots N_{sh} as indicated and noiseless optimization results are shown for comparison as the dashed line. While there is no clear order of the energies during early stages of the simulation, the final convergence is consistently improved with more shots. Notably, the error converges close to and below 10^{-3} for $N_{sh} = 2^{14}$ and 2^{16} and the fidelity f improves beyond 99.9%. The associated single-particle density matrix elements also converge to an accuracy better than 10^{-2} .

Similar noisy simulations of qubit-ADAPT VQE have been performed using the *Adadelta* optimizer, as specified in Appendix B. Generally we find the numerical results and the dependence on the number of shots to be comparable to SMO. Compared with SMO, *Adadelta* can

potentially take advantage of multiple QPUs by evaluating the gradient vector in parallel.

VII. DISCUSSION OF OPTIMAL POOL SIZE

One important factor determining the computational load of qubit-ADAPT VQE calculations is the size of the operator pool N_p . One simple strategy to reduce N_p is to strip off Pauli Z 's in the pool of operators, because they contribute negligibly to the ground state energy as pointed out in Refs. [16, 57]. This reduces N_p of the Hamiltonian commutator (HC) pool from 56 to 16 for the e_g model, and from 192 to 60 for the t_{2g} model, due to a large degeneracy. Furthermore, some qualitative guidance has been laid out in the literature to construct a minimal complete pool (MCP) of size $2(N_q - 1)$ [16, 60], where N_q is the number of qubits. Indeed, we find that a MCP can be constructed using a subset of operators in HC pool.

Nevertheless, we discover an interesting dichotomy that the reduction of pool size can potentially make the optimization of the qubit-ADAPT ansatz more challenging, especially in the presence of noise. Figure 4(a) shows the qubit-ADAPT energies with increasing N_θ from state vector simulations of the e_g model using three pools of dimension 56, 16 and 10 discussed above. All the simulations converge with 31 parameters and final CNOT gate numbers $N_{cx} = 150, 98$, and 62 that decrease for the smaller pools. The details of convergence rate of the three runs differ significantly. When the pool dimension

decreases, the region of N_θ with minimal energy change expands, as seen by the almost flat segments of the curves of Fig. 4(a). The minimal energy gain implies that small noise in the cost function evaluation could deteriorate the parameter optimization. Indeed as shown in Fig. 4(b), the qubit-ADAPT energy from noisy simulation converges slower as the pool size decreases. The flat segments in the energy curves become more evident owing to the stochastic energy errors. We further analyse the quality of the qubit-ADAPT ansatz by evaluating the energy at optimal angles obtained in noisy simulations, as plotted in Fig. 4(c). The energy difference is 0.001, 0.027, 0.135 at $N_\theta = 31$ where the state vector simulation converges, and 0.0006, 0.001, 0.005 at the end of $N_\theta = 40$ for calculations with pools of size 56, 16 and 10, respectively. Our analysis clearly shows the strikingly distinct convergence behaviors of qubit-ADAPT calculations using different complete pools in the presence of quantum shot noise. This indicates that the optimal pool in practical calculations can be a trade-off between choosing a small pool size and guaranteeing sufficient connectivity of the operators in the pool.

VIII. ESTIMATING GROUND STATE ENERGY ON NISQ DEVICE

As a further step to benchmark the realistic noise effect on qubit-ADAPT VQE calculations of the multi-orbital quantum impurity models, we measure the Hamiltonian expectation value of the e_g model with a converged qubit-ADAPT ansatz on the IBM quantum device `ibmq_casablanca`. The ansatz with optimal parameters is obtained with the HC pool using statevector simulations, as discussed in Sec. V. The converged qubit-ADAPT ansatz used for the ground state energy estimate has 32 parameters, and the associated 32 generators for multi-qubit unitary gates are listed in Appendix C. The circuits are transpiled into the basis gates of the device using the qubit layout and coupling map illustrated in the inset of Fig. 5(a). Each of the three transpiled measurement circuits for the e_g model contains about 350 CNOT gates.

To reduce the noise in the cost function measurement, it is essential to utilize a range of error mitigation techniques. We employ the standard readout error mitigation using the full confusion matrix approach, as implemented in Qiskit [42]. The adopted measurement circuits based on Hamiltonian integral factorization also allows convenient symmetry detection and filtering with respect to how well the ansatz preserves the total electron number $N_e = 4$ and total spin z-projection $S_z = 0$. The gate error is mitigated using zero noise extrapolation (ZNE) with Richardson second-order polynomial inference [61, 62]. The noise scale factor increases from 1 to 2 and 3 for each measurement circuit by local random unitary folding following the implementation in Mitiq [63, 64]. Because of the random gate folding and the stochastic SWAP mapping during transpilation to native gates [42], we

perform ten runs for each measurement circuit at each noise level to smooth out the nondeterministic effects with averaging. For each run, we apply $N_{\text{sh}} = 2^{14}$ shots for the measurements.

Figure 5(a) shows the Richardson extrapolation for the ground state energy with measured points at noise scale factors $\lambda = 1, 2, 3$, taking all ten runs for each λ into account. The estimated energy has an absolute error $\Delta(E) = 0.6 \pm 1.4$ compared with the exact result indicated by the horizontal dashed line. This corresponds to a relative error of 3%. The standard deviation is obtained by fitting the sample points with a second order polynomial using the SciPy function `curve_fit` which takes both the mean values and standard deviations into account [65]. In the postprocessing for the mean value of the energy cost function from statistical samplings, we first apply readout calibration, followed by symmetry filtering which discards the configurations with total electron number $N_e \neq 4$ or total spin $S_z \neq 0$. Interestingly, we observe that the ten runs can be divided into two groups based on the average N_e and S_z evaluated before symmetry filtering, as shown in Fig. 5(c) and (d). A subgroup of five runs denoted by square symbols have much less bias away from the correct conserved quantum numbers $N_e = 4$ and $S_z = 0$ than the other five runs shown as circles. A more accurate ground state energy can be obtained when restricting to this optimal subgroup, as shown in Fig. 5(b). The estimated energy error reduces significantly to $\Delta(E) = 0.1 \pm 0.2$, with a relative error of 0.7%.

IX. CONCLUSIONS

In an effort towards performing hybrid quantum-classical simulations of realistic correlated materials using a quantum embedding approach, we assess the gate depth and accuracy of variational ground state preparation with fixed and adaptive ansätze for two representative interacting multi-orbital, e_g and t_{2g} , impurity models. To take advantage of the sparsity of the Hamiltonian in the atomic orbital representation in real space, we consider the HVA ansatz and an adaptive variant in the qubit-encoded atomic orbital basis. A HC pool composed of pairwise commutators of the Hamiltonian terms is developed to allow fair comparison between the qubit-ADAPT and HVA ansatz. For reference, the standard UCCSD and related qubit-ADAPT calculations using UCCSD-compatible pools are also presented. The qubit-ADAPT calculation with a HC pool generally produces the most compact circuit representation with a minimal number of CNOTs in the final converged circuit. The fixed HVA ansatz follows very closely and has the additional advantage of requiring the least variational parameters N_θ .

To address the effect of quantum shot noise, we report QASM simulations of qubit-ADAPT VQE in the presence of shot noise for different numbers of shots (N_{sh}) that allows controlling the stochastic error. For our benchmark, we adopt state-of-the-art techniques such as low-

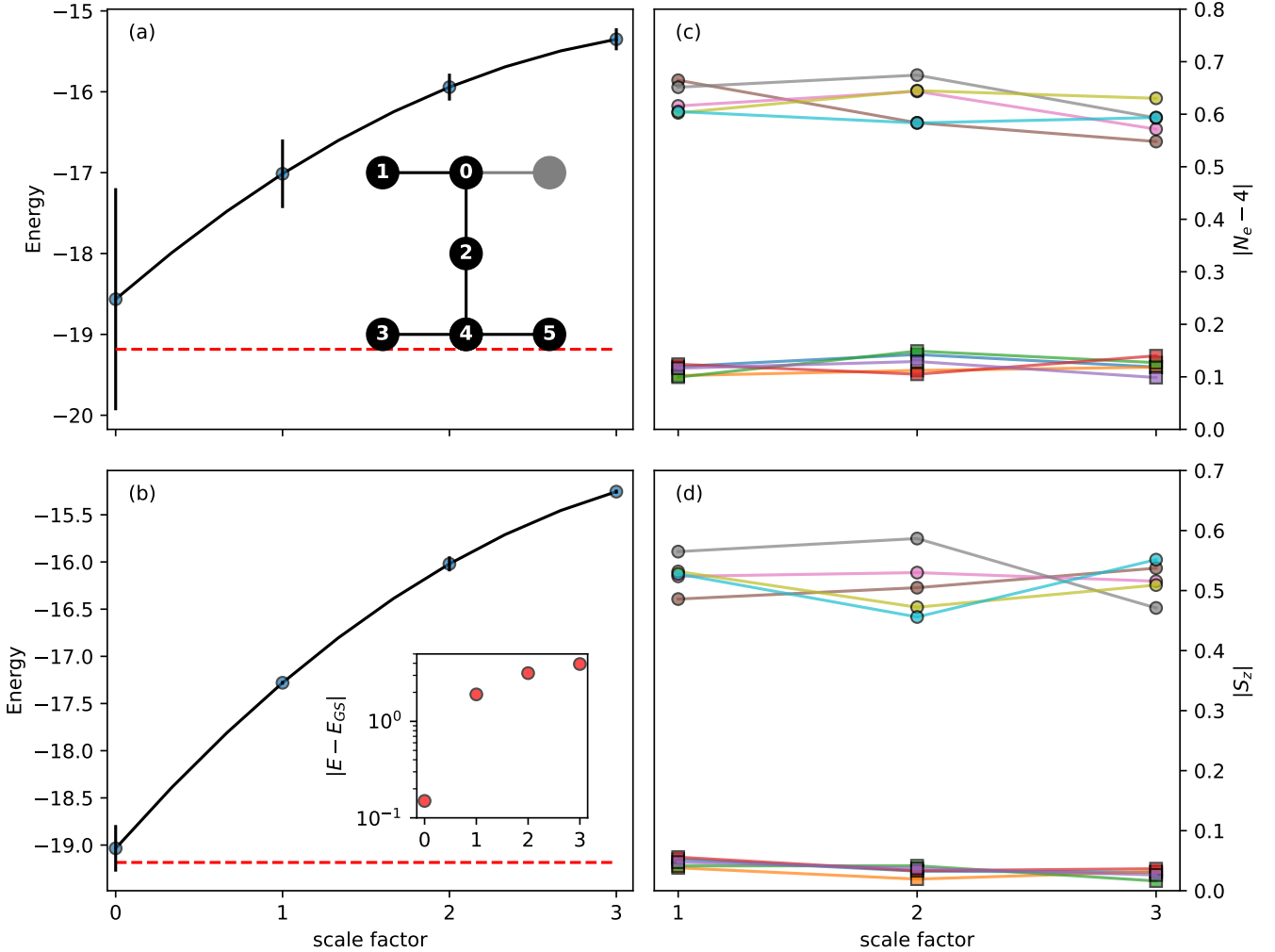


FIG. 5. **Estimating ground state energy of the e_g model on IBM device `ibmq_casablanca`.** Richardson energy extrapolation is applied by a quadratic curve fitting for three data points of increasing noise scale with averages over 10 runs in (a) and an optimal subset of 5 runs in (b). Distinct but equivalent hardware native circuits are associated with each run owing to the nondeterministic nature of local random unitary folding and transpilation. The average number of electrons N_e and total spin z-component S_z for each of the 10 runs in terms of their deviations from ideal values are plotted in (c) and (d), respectively. The optimal subset of 5 runs are identified by smaller symmetry violations $|N_e - 4| < 0.2$ and $|S_z| < 0.1$. The inset in (a) shows the qubit layout of `ibmq_casablanca`. The dark numbered circles represent the qubits adopted in the calculation with that particular order. Inset in (b): the energy error $\Delta(E) = |E - E_{GS}|$ in log scale.

rank tensor factorization to reduce the number of distinct measurement circuits and a noise resilient optimization including sequential minimal optimization and *Adadelta*. We find a modest number of shots $N_{sh} = 2^{14}$ per measurement circuit can lead to a variational representation of the ground state with fidelity $f > 99.9\%$.

We further discuss ways to simplify the pool operators and reduce the pool size using e_g model as an example. It is pointed out that a minimal complete pool, as defined in Ref. [16, 60], can be constructed using a subset of the HC pool. While a simplified pool can reduce the quantum computation resource in the adaptive operator screening procedure, it can make the classical optimization more

complicated, especially in the presence of noise. This suggests both the dimension and connectivity of operators are joint determining factors to design a practically optimal pool.

Finally, to assess the effects of realistic noise on VQE calculations of multi-orbital impurity models, we measure the ground state energy of the e_g model with a converged qubit-ADAPT ansatz on the `ibmq_casablanca` QPU. It is demonstrated that an error of 0.1 (0.7%) for the total energy can be obtained by adopting error mitigation techniques such as ZNE, combined with a careful post-selection based on symmetry and the conservation of quantum numbers.

Moving forward, the full qubit-ADAPT VQE calculations of quantum impurity models will be extended from noiseless QASM simulations to simulations that include realistic noise effects and finally to experiments on real hardware. Our study shows that an array of error mitigation techniques, including readout calibration, ZNE [61, 62], and potentially as probabilistic error cancellation [62, 66], Clifford data regression [67, 68], and probabilistic machine learning based techniques [69], need to be adopted to reach sufficiently accurate results. This is especially important when using VQE as an impurity solver in a quantum embedding approach as sufficiently accurate impurity model results are needed in order to enable convergence of the classical self-consistency loop. Our results constitute an important step forward in demonstrating high fidelity ground state preparation of impurity models on quantum devices, which is essential for realizing material simulations through hybrid quantum-classical embedding approaches.

All the codes developed by the authors for calculations and the data used to produce the figures in this work are available at figshare [38, 45, 46, 55, 70].

ACKNOWLEDGEMENTS

The authors acknowledge valuable discussions with Thomas Iadecola, Niladri Gomes, Cai-Zhuang Wang and Nicola Lanatà. This work was supported by the U.S. Department of Energy (DOE), Office of Science, Basic Energy Sciences, Materials Science and Engineering Division. The research was performed at the Ames Laboratory, which is operated for the U.S. DOE by Iowa State University under Contract No. DE-AC02-07CH11358. We acknowledge use of the IBM Quantum Experience, through the IBM Quantum Researchers Program. The views expressed are those of the authors, and do not reflect the official policy or position of IBM or the IBM Quantum team.

Appendix A: Hamiltonian factorization of the impurity model

Here we explain explicitly how the Hamiltonian factorization is obtained using the e_g model as an example, whose Hamiltonian takes the following specific form ac-

cording to Eq. (11):

$$\hat{H} = D \sum_{i=1}^2 \sum_{\sigma} \left(\hat{c}_{i\sigma}^{\dagger} \hat{f}_{i\sigma} + h.c. \right) \quad (\text{A1})$$

$$+ J/2 \left(\hat{c}_{1\uparrow}^{\dagger} \hat{c}_{2\uparrow} + \hat{c}_{1\downarrow}^{\dagger} \hat{c}_{2\downarrow} + h.c. \right)^2 \quad (\text{A2})$$

$$+ U \sum_{i=1}^2 \hat{n}_{i\uparrow} \hat{n}_{i\downarrow} + (U - 2J) \sum_{\sigma\sigma'} \hat{n}_{1\sigma} \hat{n}_{2\sigma'} \quad (\text{A3})$$

$$+ \tilde{\epsilon} \sum_{i=1}^2 \sum_{\sigma} \hat{n}_{i\sigma} + \lambda \sum_{i=1}^2 \sum_{\sigma} \hat{n}_{i\sigma}^f. \quad (\text{A4})$$

Here $\hat{n}_{i\sigma} = \hat{c}_{i\sigma}^{\dagger} \hat{c}_{i\sigma}$ and $\hat{n}_{i\sigma}^f = \hat{f}_{i\sigma}^{\dagger} \hat{f}_{i\sigma}$ are the electron occupation number operators for the physical and bath orbitals, respectively. The factorization procedure is only needed for the single-particle hybridization term (A1) and the pair hopping and spin flip terms (A2), as the rest are already in the diagonal representation.

The hybridization term (A1) can be written in a diagonal form through single-particle rotations on the physical and bath orbitals as follows:

$$\sum_{i=1}^2 \left(\hat{c}_{i\sigma}^{\dagger} \hat{f}_{i\sigma} + h.c. \right) = -\hat{n}_{1\sigma}^{(0)} - \hat{n}_{2\sigma}^{(0)} + \hat{n}_{3\sigma}^{(0)} + \hat{n}_{4\sigma}^{(0)}, \quad (\text{A5})$$

where $\hat{n}_{m\sigma}^{(0)} = \hat{c}_{m\sigma}^{\dagger(0)} \hat{c}_{m\sigma}^{(0)}$ and the rotated fermionic operators $\hat{c}_{m\sigma}^{(0)}$ are given by,

$$\begin{aligned} \hat{c}_{1\sigma}^{(0)} &= \frac{1}{\sqrt{2}} (\hat{c}_{1\sigma} + \hat{f}_{1\sigma}), \hat{c}_{2\sigma}^{(0)} = \frac{1}{\sqrt{2}} (\hat{c}_{2\sigma} + \hat{f}_{2\sigma}), \\ \hat{c}_{3\sigma}^{(0)} &= \frac{1}{\sqrt{2}} (\hat{c}_{1\sigma} - \hat{f}_{1\sigma}), \hat{c}_{4\sigma}^{(0)} = \frac{1}{\sqrt{2}} (\hat{c}_{2\sigma} - \hat{f}_{2\sigma}). \end{aligned} \quad (\text{A6})$$

This can be derived conveniently in the matrix formula-

tion:

$$\begin{aligned}
& \sum_{i=1}^2 \left(\hat{c}_{i\sigma}^\dagger \hat{f}_{i\sigma} + h.c. \right) \\
&= (\hat{c}_{1\sigma}^\dagger \hat{c}_{2\sigma}^\dagger \hat{f}_{1\sigma}^\dagger \hat{f}_{2\sigma}^\dagger) \begin{pmatrix} 0 & 0 & 1 & 0 \\ 0 & 0 & 0 & 1 \\ 1 & 0 & 0 & 0 \\ 0 & 1 & 0 & 0 \end{pmatrix} \begin{pmatrix} \hat{c}_{1\sigma} \\ \hat{c}_{2\sigma} \\ \hat{f}_{1\sigma} \\ \hat{f}_{2\sigma} \end{pmatrix} \\
&= (\hat{c}_{1\sigma}^\dagger \hat{c}_{2\sigma}^\dagger \hat{f}_{1\sigma}^\dagger \hat{f}_{2\sigma}^\dagger) \begin{pmatrix} \frac{1}{\sqrt{2}} & 0 & \frac{1}{\sqrt{2}} & 0 \\ 0 & \frac{1}{\sqrt{2}} & 0 & \frac{1}{\sqrt{2}} \\ \frac{1}{\sqrt{2}} & 0 & -\frac{1}{\sqrt{2}} & 0 \\ 0 & \frac{1}{\sqrt{2}} & 0 & -\frac{1}{\sqrt{2}} \end{pmatrix} \\
&\times \begin{pmatrix} -1 & 0 & 0 & 0 \\ 0 & -1 & 0 & 0 \\ 0 & 0 & 1 & 0 \\ 0 & 0 & 0 & 1 \end{pmatrix} \begin{pmatrix} \frac{1}{\sqrt{2}} & 0 & \frac{1}{\sqrt{2}} & 0 \\ 0 & \frac{1}{\sqrt{2}} & 0 & \frac{1}{\sqrt{2}} \\ \frac{1}{\sqrt{2}} & 0 & -\frac{1}{\sqrt{2}} & 0 \\ 0 & \frac{1}{\sqrt{2}} & 0 & -\frac{1}{\sqrt{2}} \end{pmatrix} \begin{pmatrix} \hat{c}_{1\sigma} \\ \hat{c}_{2\sigma} \\ \hat{f}_{1\sigma} \\ \hat{f}_{2\sigma} \end{pmatrix} \\
&= \left(\hat{c}_{1\sigma}^{\dagger(0)} \hat{c}_{2\sigma}^{\dagger(0)} \hat{c}_{3\sigma}^{\dagger(0)} \hat{c}_{4\sigma}^{\dagger(0)} \right) \begin{pmatrix} -1 & 0 & 0 & 0 \\ 0 & -1 & 0 & 0 \\ 0 & 0 & 1 & 0 \\ 0 & 0 & 0 & 1 \end{pmatrix} \begin{pmatrix} \hat{c}_{1\sigma}^{(0)} \\ \hat{c}_{2\sigma}^{(0)} \\ \hat{c}_{3\sigma}^{(0)} \\ \hat{c}_{4\sigma}^{(0)} \end{pmatrix}. \tag{A7}
\end{aligned}$$

The pair hopping and spin flip terms of the second line of Eq. (A2) can be rewritten as:

$$J/2 \left(\left(\hat{c}_{1\uparrow}^\dagger \hat{c}_{1\downarrow}^\dagger \hat{c}_{2\uparrow}^\dagger \hat{c}_{2\downarrow}^\dagger \right) \mathcal{L}^{(1)} \begin{pmatrix} \hat{c}_{1\uparrow} \\ \hat{c}_{1\downarrow} \\ \hat{c}_{2\uparrow} \\ \hat{c}_{2\downarrow} \end{pmatrix} \right)^2. \tag{A8}$$

with

$$\mathcal{L}^{(1)} = \begin{pmatrix} 0 & 0 & 1 & 0 \\ 0 & 0 & 0 & 1 \\ 1 & 0 & 0 & 0 \\ 0 & 1 & 0 & 0 \end{pmatrix}. \tag{A9}$$

The above expression is obtained by diagonalizing the Coulomb supermatrix of $V_{(\alpha\beta),(\gamma\delta)}$ with density-density elements set to zero, $V_{(\alpha\alpha),(\gamma\gamma)} \equiv 0$, which gives a single eigenvector associated with nonzero eigenvalue. Following the similar derivation in Eq. (A7), the pair hopping and spin flip terms have the following diagonal representation:

$$J/2 \left(-\hat{n}_{1\uparrow}^{(1)} - \hat{n}_{1\downarrow}^{(1)} + \hat{n}_{2\uparrow}^{(1)} + \hat{n}_{2\downarrow}^{(1)} \right)^2, \tag{A10}$$

with $\hat{n}_{m\sigma}^{(1)} = \hat{c}_{m\sigma}^\dagger \hat{c}_{m\sigma}^{(1)}$ and

$$\hat{c}_{1\sigma}^{(1)} = \frac{1}{\sqrt{2}}(\hat{c}_{1\sigma} + \hat{c}_{2\sigma}), \hat{c}_{2\sigma}^{(1)} = \frac{1}{\sqrt{2}}(\hat{c}_{1\sigma} - \hat{c}_{2\sigma}). \tag{A11}$$

Finally, we can represent the embedding Hamiltonian

for e_g model in the following doubly-factorized form:

$$\begin{aligned}
\hat{\mathcal{H}} &= D \sum_{\sigma} \left(-\hat{n}_{1\sigma}^{(0)} - \hat{n}_{2\sigma}^{(0)} + \hat{n}_{3\sigma}^{(0)} + \hat{n}_{4\sigma}^{(0)} \right) \\
&+ J/2 \left(-\hat{n}_{1\uparrow}^{(1)} - \hat{n}_{1\downarrow}^{(1)} + \hat{n}_{2\uparrow}^{(1)} + \hat{n}_{2\downarrow}^{(1)} \right)^2 \\
&+ U \sum_{i=1}^2 \hat{n}_{i\uparrow} \hat{n}_{i\downarrow} + (U - 2J) \sum_{\sigma\sigma'} \hat{n}_{1\sigma} \hat{n}_{2\sigma'} \\
&+ \tilde{\epsilon} \sum_{i=1}^2 \sum_{\sigma} \hat{n}_{i\sigma} + \lambda \sum_{i=1}^2 \sum_{\sigma} \hat{n}_{i\sigma}^f. \tag{A12}
\end{aligned}$$

With the Hamiltonian integral factorization we find that three distinct measurement circuits are needed for the Hamiltonian expectation value: (i) the diagonal terms in the original atomic orbital basis, (ii) the hybridization terms in the basis of $c_{m\sigma}^{(0)}$ (A6), (iii) the pair hopping and spin flip terms in the basis of $c_{m\sigma}^{(1)}$ (A11).

Appendix B: Quantum Simulation with Adadelta optimizer

In section VI we reported the qubit-ADAPT VQE calculation with shots using the SMO optimizer. Here we additionally perform the calculations using the *Adadelta* optimization method, which is potentially tolerant to cost function errors [71]. Below we describe the implementation of the algorithm followed by the results.

The algorithm minimizes the cost function along the steepest decent direction in parameter space, with a parameter update at step t as $\boldsymbol{\theta}_t = \boldsymbol{\theta}_{t-1} - \mathbf{w}_t \odot \mathbf{g}_t$. The gradient vector is determined from the derivative of the energy function along every parameter direction $\mathbf{g}_t = \nabla_{\boldsymbol{\theta}} E(\boldsymbol{\theta}_t)$, where $E(\boldsymbol{\theta}) = \langle \Psi[\boldsymbol{\theta}] | \hat{\mathcal{H}} | \Psi[\boldsymbol{\theta}] \rangle$ is the estimated energy. The set of parameter-dependent adaptive learning rates are determined as $\mathbf{w}_t = \frac{\sqrt{\Delta\boldsymbol{\theta}_{t-1} + \epsilon}}{\sqrt{\mathbf{s}_t + \epsilon}}$, where the leaked average of the square of rescaled gradients at the previous step is obtained as $\Delta\boldsymbol{\theta}_{t-1} = \beta\Delta\boldsymbol{\theta}_{t-2} + (1 - \beta)(\mathbf{w}_{t-1} \odot \mathbf{g}_{t-1})^2$, and that of gradients is evaluated as $\mathbf{s}_t = \beta\mathbf{s}_{t-1} + (1 - \beta)\mathbf{g}_t^2$. The operator \odot denotes element-wise product. The *Adadelta* algorithm involves a hyperparameter ϵ to regularize the ratio in determining \mathbf{w}_t , which is set to 10^{-8} , and a mixing parameter set to $\beta = 0.9$. The leaked averages are all initialized to zero. We fix the number of steps in *Adadelta* optimization to $N_s = 250$ in our simulations. Considering that the evaluation of one gradient component associated with a variational parameter involves cost function measurements at two distinct parameter points following the parameter-shift rule, the quantum computational resource for *Adadelta* optimization is comparable to SMO with $N_{\text{sw}} = 60$.

Figure 6 shows the representative convergence behavior of qubit-ADAPT energy with increasing number of variational parameters $N_{\boldsymbol{\theta}}$ calculated using number of shots $N_{\text{sh}} = 2^{16}$ per observable. The adaptive ansatz energy E decreases as the circuit depth increases with

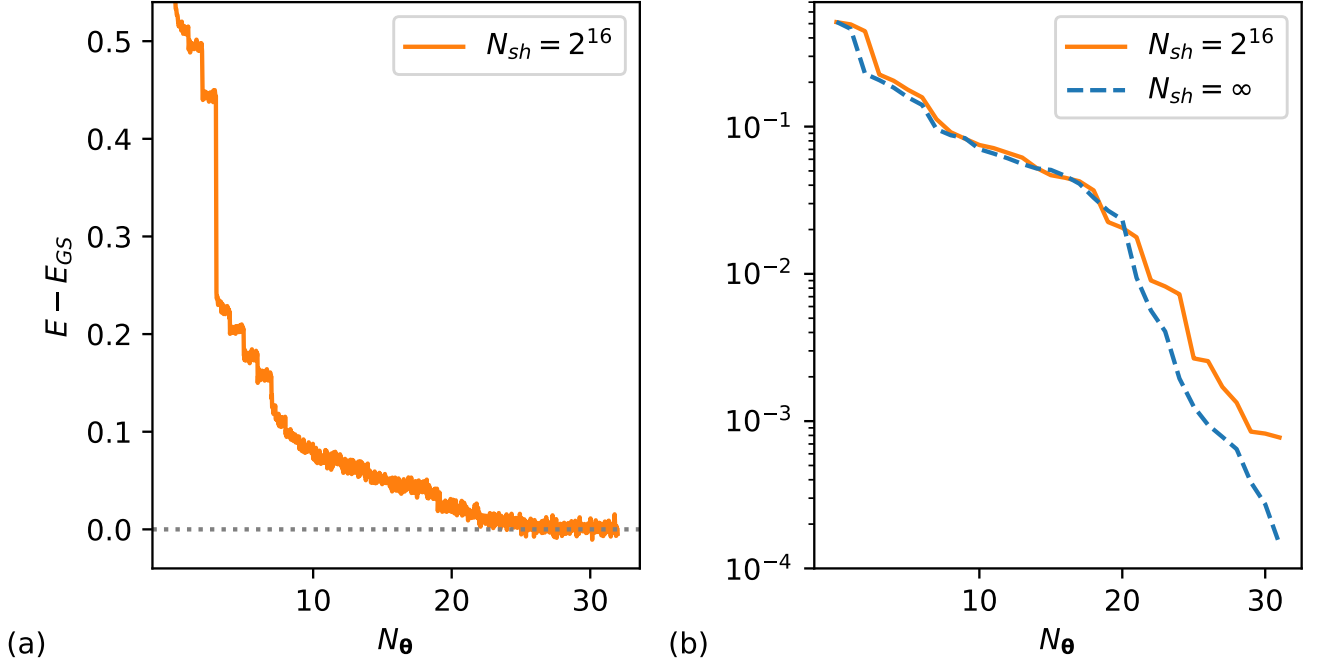


FIG. 6. **Energy convergence of qubit-ADAPT VQE noisy simulations of $(2, 2)$ e_g model with *Adadelta* optimizer.** The difference between the exact ground state energy E_{GS} and qubit-ADAPT VQE noisy simulation results, obtained with number of shots $N_{sh} = 2^{16}$ in panel (a). The energy differences evaluated using state vector for the adaptive ansätze obtained in the noisy simulations with $N_{sh} = 2^{16}$ are shown in panel (b). The state vector simulation results ($N_{sh} = \infty$) of the qubit-ADAPT VQE are also shown in dashed line for reference.

more variational parameters. The energy points shown include not only final *Adadelta* optimized energies of the qubit-ADAPT ansatz with N_{θ} parameters, but also intermediate energies for the 250 *Adadelta* steps to provide a detailed view of the convergence. For the operator screening step of the qubit-ADAPT calculation we fix $N_{sh} = 2^{16}$ for energy evaluations in all cases, and determine the energy gradient by the parameter-shift rule [59]. The final energy error from the calculations with *Adadelta* is $E - E_{GS} = 4.4 \times 10^{-3}$. This is comparable with the result from SMO optimizer.

Appendix C: The ground state ansatz of $(2, 2)$ e_g model used on `ibmq_casablanca`

The qubit-ADAPT ansatz takes the pseudo-Trotter form (8). The converged ansatz for the e_g model which

we used for the calculations on IBM quantum hardware `ibmq_casablanca` is composed of 32 generators for the multi-qubit unitary gates, which are listed here with parity encoding (in the order that they appear in the ansatz):

IIZXY, IYXIII, XYZIII, IIIZYXZ, IXYIII,
 ZXYIIZ, XYIIZZ, XYIIIIZ, IIIIYX, IZXYXX,
 IIXZYI, IIXIY, IIXIZY, IIZYXZ, IIIZYX,
 YXIII, IZZIZY, IIXIZY, IIYIIX, IIZXYI,
 IZXYXX, IZYIZX, ZYXIII, ZYIIZX, IIYIIX,
 IIIIXY, IIXIY, IIXIYZ, IIXZYI, YXXIZX,
 IIXIYZ, YXXIIX.

[1] A. Aspuru-Guzik, A. D. Dutoi, P. J. Love, and M. Head-Gordon, *Science* **309**, 1704 (2005).
 [2] A. Peruzzo, J. McClean, P. Shadbolt, M.-H. Yung, X.-Q. Zhou, P. J. Love, A. Aspuru-Guzik, and J. L. O’Brien, *Nat. Commun.* **5**, 1 (2014).
 [3] A. Kandala, A. Mezzacapo, K. Temme, M. Takita, M. Brink, J. M. Chow, and J. M. Gambetta, *Nature* **549**, 242 (2017).
 [4] P. J. O’Malley, R. Babbush, I. D. Kivlichan, J. Romero, J. R. McClean, R. Barends, J. Kelly, P. Roushan, A. Tran-

ter, N. Ding, *et al.*, Phys. Rev. X **6**, 031007 (2016).

[5] J. Preskill, Quantum **2**, 79 (2018).

[6] S. McArdle, S. Endo, A. Aspuru-Guzik, S. C. Benjamin, and X. Yuan, Rev. Mod. Phys. **92**, 015003 (2020).

[7] M. Cerezo, A. Arrasmith, R. Babbush, S. C. Benjamin, S. Endo, K. Fujii, J. R. McClean, K. Mitarai, X. Yuan, L. Cincio, *et al.*, Nature Reviews Physics **3**, 625 (2021).

[8] J. R. McClean, J. Romero, R. Babbush, and A. Aspuru-Guzik, New J. Phys. **18**, 023023 (2016).

[9] M. R. Hoffmann and J. Simons, The Journal of chemical physics **88**, 993 (1988).

[10] R. J. Bartlett, S. A. Kucharski, and J. Noga, Chemical physics letters **155**, 133 (1989).

[11] R. J. Bartlett and M. Musiał, Rev. Mod. Phys. **79**, 291 (2007).

[12] J. Romero, R. Babbush, J. R. McClean, C. Hempel, P. J. Love, and A. Aspuru-Guzik, Quantum Sci. Technol. **4**, 014008 (2018).

[13] H. R. Grimsley, S. E. Economou, E. Barnes, and N. J. Mayhall, Nat. Commun. **10**, 3007 (2019).

[14] I. G. Ryabinkin, T.-C. Yen, S. N. Genin, and A. F. Izmaylov, J. Chem. Theory Comput. **14**, 6317 (2018).

[15] J. Lee, W. J. Huggins, M. Head-Gordon, and K. B. Whaley, J. Chem. Theory Comput. **15**, 311 (2018).

[16] H. L. Tang, V. Shkolnikov, G. S. Barron, H. R. Grimsley, N. J. Mayhall, E. Barnes, and S. E. Economou, PRX Quantum **2**, 020310 (2021).

[17] F. Zhang, N. Gomes, N. F. Berthelsen, P. P. Orth, C.-Z. Wang, K.-M. Ho, and Y.-X. Yao, Physical Review Research **3**, 013039 (2021).

[18] N. Gomes, A. Mukherjee, F. Zhang, T. Iadecola, C.-Z. Wang, K.-M. Ho, P. P. Orth, and Y.-X. Yao, Adv. Quantum Technol. **4**, 2100114 (2021).

[19] D. A. Fedorov, B. Peng, N. Govind, and Y. Alexeev, Materials Theory **6**, 2 (2022).

[20] J. Tilly, H. Chen, S. Cao, D. Picozzi, K. Setia, Y. Li, E. Grant, L. Wossnig, I. Runger, G. H. Booth, and J. Tennyson, “The variational quantum eigensolver: a review of methods and best practices,” (2021), arXiv:2111.05176 [quant-ph].

[21] D. Wecker, M. B. Hastings, and M. Troyer, Phys. Rev. A **92**, 042303 (2015).

[22] W. W. Ho and T. H. Hsieh, SciPost Phys. **6**, 29 (2019).

[23] R. Wiersema, C. Zhou, Y. de Sereville, J. F. Carrasquilla, Y. B. Kim, and H. Yuen, PRX Quantum **1**, 020319 (2020).

[24] P. R. Kent and G. Kotliar, Science **361**, 348 (2018).

[25] A. Georges, G. Kotliar, W. Krauth, and M. J. Rozenberg, Rev. Mod. Phys. **68**, 13 (1996).

[26] G. Kotliar, S. Y. Savrasov, K. Haule, V. S. Oudovenko, O. Parcollet, and C. Marianetti, Rev. Mod. Phys. **78**, 865 (2006).

[27] Q. Sun and G. K.-L. Chan, Acc. Chem. Res. **49**, 2705 (2016).

[28] G. Knizia and G. K.-L. Chan, Physical Review Letters **109**, 186404 (2012).

[29] N. Lanatà, Y. Yao, X. Deng, V. Dobrosavljević, and G. Kotliar, Phys. Rev. Lett. **118**, 126401 (2017).

[30] T.-H. Lee, T. Ayral, Y.-X. Yao, N. Lanata, and G. Kotliar, Phys. Rev. B **99**, 115129 (2019).

[31] Y. Yao, F. Zhang, C.-Z. Wang, K.-M. Ho, and P. P. Orth, Phys. Rev. Research **3**, 013184 (2021).

[32] J. Bünenmann, W. Weber, and F. Gebhard, Phys. Rev. B **57**, 6896 (1998).

[33] M. Fabrizio, Phys. Rev. B **76**, 165110 (2007).

[34] X. Deng, X. Dai, and Z. Fang, EPL (Europhysics Letters) **83**, 37008 (2008).

[35] N. Lanata, Y.-X. Yao, C.-Z. Wang, K.-M. Ho, J. Schmalian, K. Haule, and G. Kotliar, Phys. Rev. Lett. **111**, 196801 (2013).

[36] F. Lu, J. Zhao, H. Weng, Z. Fang, and X. Dai, Phys. Rev. Lett. **110**, 096401 (2013).

[37] N. Lanatà, Y.-X. Yao, C.-Z. Wang, K.-M. Ho, and G. Kotliar, Phys. Rev. X **5**, 011008 (2015).

[38] Y.-X. Yao, <http://doi.org/10.6084/m9.figshare.11987616> (2020).

[39] G. Kotliar and A. E. Ruckenstein, Phys. Rev. Lett. **57**, 1362 (1986).

[40] J. Bünenmann and F. Gebhard, Phys. Rev. B **76**, 193104 (2007).

[41] N. Lanatà, H. U. R. Strand, G. Giovannetti, B. Hellsing, L. de' Medici, and M. Capone, Phys. Rev. B **87**, 045122 (2013).

[42] H. Abraham, I. Y. Akhalwaya, G. Aleksandrowicz, T. Alexander, G. Alexandrowics, E. Arbel, A. Asfaw, C. Azaustre, AzizNgoueya, P. Barkoutsos, G. Barron, L. Bello, Y. Ben-Haim, D. Bevenius, *et al.*, “Qiskit: An open-source framework for quantum computing,” (2019).

[43] T. Stein, T. M. Henderson, and G. E. Scuseria, J. Chem. Phys. **140**, 214113 (2014).

[44] T. M. Henderson, I. W. Bulik, and G. E. Scuseria, J. Chem. Phys. **142**, 214116 (2015).

[45] Y. Yao, (2022), 10.6084/m9.figshare.19350509.

[46] Y. Yao and J. C. Getelina, (2022), 10.6084/m9.figshare.19349846.

[47] S. McArdle, T. Jones, S. Endo, Y. Li, S. C. Benjamin, and X. Yuan, npj Quantum Inf. **5**, 75 (2019).

[48] A. F. Izmaylov, T.-C. Yen, R. A. Lang, and V. Verteletskyi, Journal of Chemical Theory and Computation **16**, 190 (2019).

[49] P. Gokhale, O. Angiuli, Y. Ding, K. Gui, T. Tomesh, M. Suchara, M. Martonosi, and F. T. Chong, arXiv preprint arXiv:1907.13623 (2019).

[50] A. Zhao, A. Tranter, W. M. Kirby, S. F. Ung, A. Miyake, and P. J. Love, Physical Review A **101**, 062322 (2020).

[51] O. Crawford, B. v. Straaten, D. Wang, T. Parks, E. Campbell, and S. Brierley, Quantum **5**, 385 (2021).

[52] T.-C. Yen and A. F. Izmaylov, PRX Quantum **2**, 040320 (2021).

[53] W. J. Huggins, J. R. McClean, N. C. Rubin, Z. Jiang, N. Wiebe, K. B. Whaley, and R. Babbush, npj Quantum Information **7**, 1 (2021).

[54] K. M. Nakanishi, K. Fujii, and S. Todo, Physical Review Research **2**, 043158 (2020).

[55] A. Mukherjee and Y. Yao, (2022), 10.6084/m9.figshare.19351952.

[56] D. Claudino, J. Wright, A. J. McCaskey, and T. S. Humble, Frontiers in Chemistry **8**, 1152 (2020).

[57] Y. S. Yordanov, V. Armaos, C. H. Barnes, and D. R. Arvidsson-Shukur, Communications Physics **4**, 1 (2021).

[58] X. Bonet-Monroig, H. Wang, D. Vermetten, B. Senjean, C. Moussa, T. Bäck, V. Dunjko, and T. E. O'Brien, arXiv:2111.13454 (2021).

[59] A. Mari, T. R. Bromley, and N. Killoran, Phys. Rev. A **103**, 012405 (2021).

[60] V. Shkolnikov, N. J. Mayhall, S. E. Economou, and E. Barnes, arXiv preprint arXiv:2109.05340 (2021).

[61] Y. Li and S. C. Benjamin, Phys. Rev. X **7**, 021050 (2017).

- [62] K. Temme, S. Bravyi, and J. M. Gambetta, *Phys. Rev. Lett.* **119**, 180509 (2017).
- [63] R. LaRose, A. Mari, P. J. Karalekas, N. Shammah, and W. J. Zeng, arXiv:2009.04417 (2020).
- [64] T. Giurgica-Tiron, Y. Hindy, R. LaRose, A. Mari, and W. J. Zeng, in *2020 IEEE International Conference on Quantum Computing and Engineering (QCE)* (IEEE, 2020) pp. 306–316.
- [65] P. Virtanen, R. Gommers, T. E. Oliphant, M. Haberland, T. Reddy, D. Cournapeau, E. Burovski, P. Peterson, W. Weckesser, J. Bright, *et al.*, *Nat. Methods* **17**, 261 (2020).
- [66] S. Endo, S. C. Benjamin, and Y. Li, *Phys. Rev. X* **8**, 031027 (2018).
- [67] P. Czarnik, A. Arrasmith, P. J. Coles, and L. Cincio, *Quantum* **5**, 592 (2021).
- [68] A. Lowe, M. H. Gordon, P. Czarnik, A. Arrasmith, P. J. Coles, and L. Cincio, *Phys. Rev. Research* **3**, 033098 (2021).
- [69] J. Rogers, G. Bhattacharyya, M. S. Frank, T. Jiang, O. Christiansen, Y.-X. Yao, and N. Lanatà, arXiv preprint arXiv:2111.08814 (2021).
- [70] A. Mukherjee, N. Berthelsen, J. C. Getelina, P. P. Orth, and Y. Yao, (2022), 10.6084/m9.figshare.19352222.
- [71] M. D. Zeiler, arXiv preprint arXiv:1212.5701 (2012).